

## Article

# High-Temperature-Resistant Scale Inhibitor Polyaspartic Acid-Prolineamide for Inhibiting CaCO<sub>3</sub> Scale in Geothermal Water and Speculation of Scale Inhibition Mechanism

Jiawei Yan <sup>1,2,3</sup>, Xiao Tan <sup>1</sup> and Suitao Qi <sup>1,\*</sup>

<sup>1</sup> Shaanxi Key Laboratory of Chemical Process Intensification, School of Chemical Engineering and Technology, Xi'an Jiaotong University, Xi'an 710049, China

<sup>2</sup> Science and Technology on Aerospace Chemical Power Laboratory, Xiangyang 441003, China

<sup>3</sup> Hubei Institute of Aerospace Chemotechnology, Xiangyang 441003, China

\* Correspondence: [suitaoqi@mail.xjtu.edu.com](mailto:suitaoqi@mail.xjtu.edu.com); Tel.: +86-158-0920-1586

**Abstract:** An excellent high-temperature-resistant scale inhibitor, polyaspartic acid-prolineamide (PASP-Pro), was synthesized by polysuccinimide (PSI) and L-prolineamide (L-Pro), and then characterized by <sup>1</sup>H-NMR and FTIR analysis. The inhibition performance of PASP-Pro on CaCO<sub>3</sub> precipitation was studied at different temperatures through static tests; at the same time, the influence of PASP-Pro on the crystallization process of CaCO<sub>3</sub> was investigated by combining the electrical conductivity test of CaCO<sub>3</sub> solution with different CaCO<sub>3</sub> scale characterizations. The suitable synthesis and evaluation conditions for PASP-Pro were obtained, and a possible multi-stage scale inhibition mechanism of PASP-Pro for CaCO<sub>3</sub> scale was then suggested. PASP-Pro has better thermal stability and high-temperature scale inhibition performance (exceeds 87% after pretreatment at 150 °C) than PASP. In addition, PASP-Pro exhibited a promising anti-scaling property by inhibiting the crystallization of CaCO<sub>3</sub>; the induction period and the nucleation period of the CaCO<sub>3</sub> crystallization process were prolonged nearly four times. It was found from XRD patterns that vaterite, an unstable crystalline phase, gradually emerged with the addition of the scale inhibitors, and the aragonite crystals are clearly observed in SEM images. Finally, the possible multi-stage scale inhibition mechanism of PASP-based inhibitors was proposed, including coating impurities, electrostatic repulsion, and inhibiting dehydration and rearrangement of CaCO<sub>3</sub> crystallization.

**Keywords:** polyaspartic acid; phosphorus-free; high temperature resistant; scale inhibition mechanism



**Citation:** Yan, J.; Tan, X.; Qi, S. High-Temperature-Resistant Scale Inhibitor Polyaspartic Acid-Prolineamide for Inhibiting CaCO<sub>3</sub> Scale in Geothermal Water and Speculation of Scale Inhibition Mechanism. *Water* **2023**, *15*, 1457. <https://doi.org/10.3390/w15081457>

Academic Editor: Licínio M. Gando-Ferreira

Received: 15 February 2023

Revised: 15 March 2023

Accepted: 4 April 2023

Published: 8 April 2023



**Copyright:** © 2023 by the authors. Licensee MDPI, Basel, Switzerland. This article is an open access article distributed under the terms and conditions of the Creative Commons Attribution (CC BY) license (<https://creativecommons.org/licenses/by/4.0/>).

## 1. Introduction

Geothermal resources refer to the renewable heat energy stored in the earth, they have outstanding characteristics such as wide distribution and direct utilization, and are recyclable and pollution free [1–3]. Geothermal resources have been widely used in power generation, heating exchange, etc. [3–6], which has produced huge economic benefits to human society. Geothermal water is the most common carrier of geothermal energy; however, being rich in calcium ions, it easily forms calcium scale due to the sedimentation of calcium salts. CaCO<sub>3</sub> is one of the most common types of scale in geothermal water [7]. When the concentration of Ca<sup>2+</sup> and CO<sub>3</sub><sup>2-</sup> in the geothermal water exceeds the solubility product constant (K<sub>sp</sub>) of CaCO<sub>3</sub>, the unstable supersaturated CaCO<sub>3</sub> solution forms and easily crystallizes under external shocks or introduced seed crystals. Moreover, CaCO<sub>3</sub> deposition becomes more serious at high temperatures due to the solubility of CaCO<sub>3</sub> decreasing with the increase in temperature. Such scaling in the pipeline inevitably increases the thermal resistance and causes pipeline blockage [8,9], thus restricting the long-term normal operation of the geothermal water system.

Adding scale inhibitors is one of the most effective ways to inhibit CaCO<sub>3</sub> scale formation in geothermal water [10]. As one of the most frequently used inhibitors in high-temperature applications, organic phosphonate scale inhibitors have the risk of causing

eutrophication of water after decomposition [11]. As a result, the design of environmentally friendly chemicals has become a pressing task and a requirement of scale inhibitors.

Currently, the most promising alternative to conventional organic phosphonate scale inhibitors are phosphorus-free polyaspartic acid (PASP)-based inhibitors. PASP-based inhibitors exhibit an excellent scale inhibition effect on  $\text{CaCO}_3$  owing to their large number of carboxylic acid groups in the molecular chain. On the other hand, they can be completely degraded by microorganisms into harmless small molecules (carbon dioxide, water, etc.) [10]. However, PASP loses its anti-scaling performance dramatically when exposed to high temperatures, which severely restricts the application of PASP [12–14].

Chemical modification by grafting small molecules on the side chain is an effective method to change the polarity, crystallinity, and thermal stability of PASP. Therefore, a modified PASP with temperature-resistant properties can be synthesized through the selection of stable heterocyclic monomers. Xu et al. prepared a polyaspartic acid/5-aminoorotic acid graft copolymer (PASP/5-AOA) and found its scale inhibition rate for  $\text{CaCO}_3$  exceeded 85% at 80 °C for 16 h [12]. Shi et al. selected a corrosion-resistant heterocyclic molecule and synthesized a polyaspartic acid/furfurylamine graft copolymer (PASP-FA); its scale inhibition performance was 10% higher than PASP at 80 °C after 18 h [13].

In general, for the  $\text{CaCO}_3$  crystallization process, amorphous calcium carbonate (ACC) is formed first, and then converted into thermodynamically stable polycrystals including calcite, aragonite, and vaterite through different pathways. For example, a transformation mechanism from hydrated ACC via a short-lived anhydrous ACC to the final polymorph was suggested where the crystalline phase propagates via secondary nucleation from one domain to its neighbor [15–17]. However, the crystal nucleus size is very small, and its formation speed is extremely fast, which makes it difficult to obtain a detailed description of the  $\text{CaCO}_3$  crystallization process. With the development of observation technology and computational chemistry, a more generally accepted mechanism is the multi-stage nucleation process of  $\text{CaCO}_3$ , which has been proposed. This process can be divided into the following stages [18–20]: (1) Formation of amorphous ionic liquid.  $\text{Ca}^{2+}$  and  $\text{CO}_3^{2-}$  ions are alternately arranged to form a highly disordered, flexible, and hydrated dynamic topological structure composed of chains, branches, and rings. (2) Formation of ACC. Amorphous ionic liquids will collapse and aggregate into 3D ACC spherical particles during the dynamic process of formation and dissipation, and the local dehydration sequence results in a more orderly structure at the same time. (3) Transformation into a more stable crystal form. There are two kinds of viewpoints on this process: one is the dissolution precipitation model (Ostwald–Lussac rule of stages), in which ACC precursors are redissolved on the stable crystal surface before precipitation; the other is ACC precursors directly convert into stable crystalline phases based on the continuous contact between the old and new phases.

The addition of scale inhibitors can significantly inhibit the crystallization of  $\text{CaCO}_3$ . To the best of our knowledge, there are some existing inhibiting mechanisms such as threshold effect, chelating, lattice distortion, adsorption, and dispersion during the  $\text{CaCO}_3$  crystallization process [21–24]; however, they are mainly summarized from experimental phenomena. Obviously, it is necessary to explore a dynamic anti-scaling mechanism at the micro level, which may be more instructive to explain how the scale inhibitors work.

In this work, L-prolinamide with a five-membered heterocyclic was selected to synthesize the phosphorus-free scale inhibitor PASP-Pro, and its structure was characterized by FTIR and NMR. The anti-scale property of PASP-Pro against  $\text{CaCO}_3$  precipitation was studied by static scale inhibition tests and electrical conductivity tests. The change in  $\text{CaCO}_3$  scales, with or without the addition of an inhibitor, was investigated by XRD and SEM to clarify the anti-scaling mechanism.

## 2. Materials and Methods

### 2.1. Materials and Instruments

The chemicals involved in this work were purchased from Sinopharm Chemical Reagent Co. Ltd. (Shanghai, China), including maleic anhydride, urea, sulfuric acid, phosphonic acid, N, N-dimethylformamide, L-Prolinamide, sodium carbonate, sodium bicarbonate, and calcium chloride. The standard polyaspartic acid (PASP, 40 wt% aqueous solution) was purchased from Yuanye Biotechnology Co. Ltd. (Shanghai, China).

The instruments involved are a conductivity meter (DDSJ-308A, Shanghai INESA Scientific Instrument Co., Ltd, Shanghai, China), ion chromatograph (DIONEX INTEGRION, American Thermo Company, Waltham, MA, USA), Fourier-infrared transform spectrometer (Nicolet iS 50, American Thermo Fisher Scientific Company, Waltham, MA, USA), nuclear magnetic resonance spectrometer (AVANCE III HD 600 MHz, Switzerland), scanning electron microscope (MALA3LMH, Czech TESCABN Company, Tescabn, Czech), and X-ray diffractometer (XRD-6100, Japan Shimadzu Company, Kyoto, Japan).

### 2.2. Synthesis of PASP and PASP-Pro

Polysuccinimide (PSI) was synthesized in our laboratory according to the maleic anhydride method [25,26]. An amount of 2.0 g of PSI and 10.0 mL 2.5 M of sodium hydroxide were placed in a round bottom flask to start a ring-opening reaction at 333 K under an alkaline environment of sodium hydroxide for a certain time; then, the mixture was poured into enough dehydrated ethanol to produce a precipitate. After vacuum drying at 333 K, a light-yellow solid of PASP was obtained.

Similarly, 2.0 g PSI, 1.5 g L Pro, and 10.0 mL of ultrapure water were mixed in a round bottom flask at 333 K for 6 h; then, 5.0 mL of 2.5 M sodium hydroxide was slowly added to the mixture, and the ring-opening reaction was carried for a certain time. After performing the same separation steps as in the PASP preparation, a brown-yellow solid of PASP-Pro was obtained. The relevant synthesized route is expressed in Figure 1.

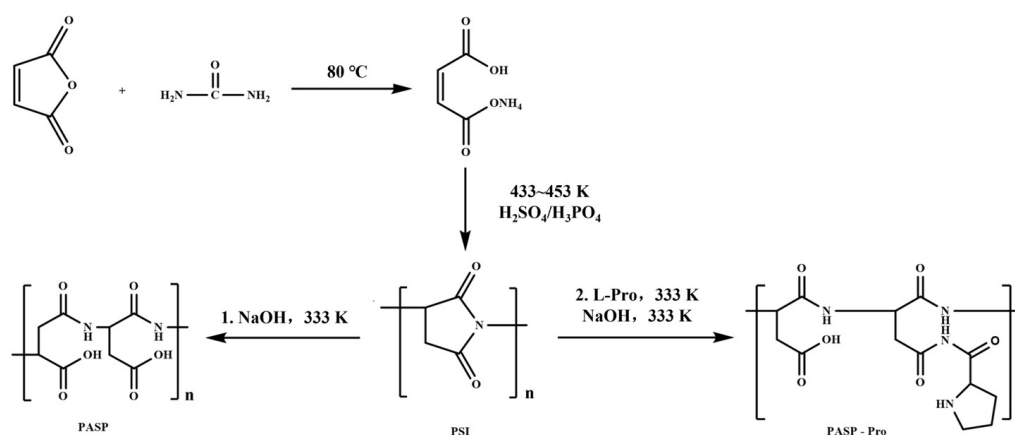


**Figure 1.** Synthesis routes of PASP and PASP-Pro copolymers.  $n$ , represents the repeating units of the polymers.

### 2.3. Static Anti-Scaling Test of $\text{CaCO}_3$

The anti-scaling performance of  $\text{CaCO}_3$  was tested according to the China National Standard (GB/T 16632-2019) [27].  $\text{CaCl}_2$  solution, scale inhibitor (or equal amount of ultrapure water), and  $\text{NaHCO}_3$  solution were successively added into the flask to prepare an artificial solution, where  $\rho(\text{Ca}^{2+}) = 240\text{ mg/L}$  and  $\rho(\text{HCO}_3^-) = 732\text{ mg/L}$ . A series of different 250 mL artificial solutions were kept at  $80\text{ }^\circ\text{C}$  in a water bath for 10 h. Then, they were cooled to room temperature and filtered, and the remaining  $\text{Ca}^{2+}$  concentration in the supernatant was tested by ion chromatography. Before the test, the  $\text{Ca}^{2+}$  standard curve (from 0~100 mg/L) was made with the  $\text{Ca}^{2+}$  standard solution. Then, the solutions before and after the static test were diluted to the appropriate concentration (10~50 mg/L) with

ultrapure water, and the  $\text{Ca}^{2+}$  concentration was measured twice to ensure experimental accuracy. The scale inhibition rate ( $\eta$ ) was calculated by the following Equation (1):

$$\eta = (c_1 - c_2)/(c_0 - c_2) \times 100\%, \quad (1)$$

where  $c_0$  is the concentration of  $\text{Ca}^{2+}$  before the static test,  $c_1$  is the concentration of  $\text{Ca}^{2+}$  after the static test when adding the inhibitor, and  $c_2$  is the concentration of  $\text{Ca}^{2+}$  after the static test where there is no inhibitor.

The inhibition performance of PASP and PASP-Pro on  $\text{CaCO}_3$  was tested under different ring-opening times, concentrations, pHs, and  $\text{Ca}^{2+}$  concentrations to obtain the most suitable conditions for the synthesis and evaluation of scale inhibitors. In addition, the effect of bath temperatures and bath time were carried out to explore the improvement of scale inhibition performance at high temperatures. To verify that PASP-Pro could maintain highly efficient performance at high temperatures, PASP-Pro was pretreated in a hydrothermal kettle in the temperature range of 110 °C to 170 °C for 3 h before static testing.

#### 2.4. Analysis of Crystal Nucleation and Growth Processes

The electric conductivity of the  $\text{CaCO}_3$  supersaturated solution, which was composed of 2.0 mL 0.10 M  $\text{CaCl}_2$  solution, 2.0 mL 0.10 M  $\text{Na}_2\text{CO}_3$  solution, 50 mL ultrapure water, and different scale inhibitors (20 mg/L), was recorded by an electric conductivity meter. The effect of the scale inhibitors on the induction period, nucleation period, and growth period of  $\text{CaCO}_3$  crystals are reflected by the change in the conductivity value [28].

#### 2.5. Formation and Characterization of Different $\text{CaCO}_3$ Scales

Equal volumes of  $\text{CaCl}_2$ ,  $\text{NaHCO}_3$  solution, and the proper scale inhibitor (or an equal amount of ultrapure water) were mixed in a beaker with a magnetic stirrer to form the corresponding  $\text{CaCO}_3$  scales. The prepared  $\text{CaCO}_3$  crystals were harvested at room temperature for 24 h and washed with enough ultrapure water to remove the residual scale inhibitors.

X-ray diffraction spectrum (XRD) using  $\text{Cu K}\alpha$  radiation and scanning electron microscopy (SEM) were used to characterize the formed  $\text{CaCO}_3$  scales under the different scale inhibitors. XRD data were collected from 10~80° with a scanning rate of 10°/min. A thin layer of gold was sprayed on the different scale surfaces and then their images were recorded by scanning electron microscopy (SEM) at 10 kV working voltage.

### 3. Results and Discussion

#### 3.1. FTIR, $^1\text{H}$ NMR, and GPC Analysis of PASP-Pro

The FTIR spectra were used to characterize the structures of PSI, L-Pro, PASP, and PASP-Pro. The characteristic peaks of PSI (Figure 2a) at 1354  $\text{cm}^{-1}$  (C-N), 1656  $\text{cm}^{-1}$  (C=O), 1716  $\text{cm}^{-1}$  (related to linked carbonyl coupling effect), and 2951  $\text{cm}^{-1}$  (C-H stretching vibration) reveal that PSI was successfully synthesized [25,29]. PASP, from the ring-opening reaction of PSI in alkaline condition, shows C=O stretching vibration peaks at 1638  $\text{cm}^{-1}$  and 1560  $\text{cm}^{-1}$ , which are derived from the carboxylic acid group (-COOH) and amide group (CO-NH), respectively. The peak at 1388  $\text{cm}^{-1}$  stands for the C-N stretching vibration (Figure 2b). Similarly, PASP-Pro shows -CH<sub>2</sub> peaks to L-Pro at 2968  $\text{cm}^{-1}$  and 2873  $\text{cm}^{-1}$ . Moreover, the amide peak at 1560  $\text{cm}^{-1}$  is significantly enhanced, which is attributed to the presence of more amide groups in PASP-Pro.

Figure 3 is the  $^1\text{H}$  NMR spectra of the synthesized PASP, PASP-Pro, and standard PASP in  $\text{CDCl}_3$ . The signals of the synthesized PASP are consistent with the standard PASP, the peak of which at 1.25 ppm and 2.58 ppm are assigned to -CH<sub>2</sub>- and -CH- of PASP main chains, respectively. A new peak at 3.74 ppm that emerges in the  $^1\text{H}$  NMR spectra of PASP-Pro is attributed to the CO-CH<sub>2</sub>-NH on the ring of L-Pro.

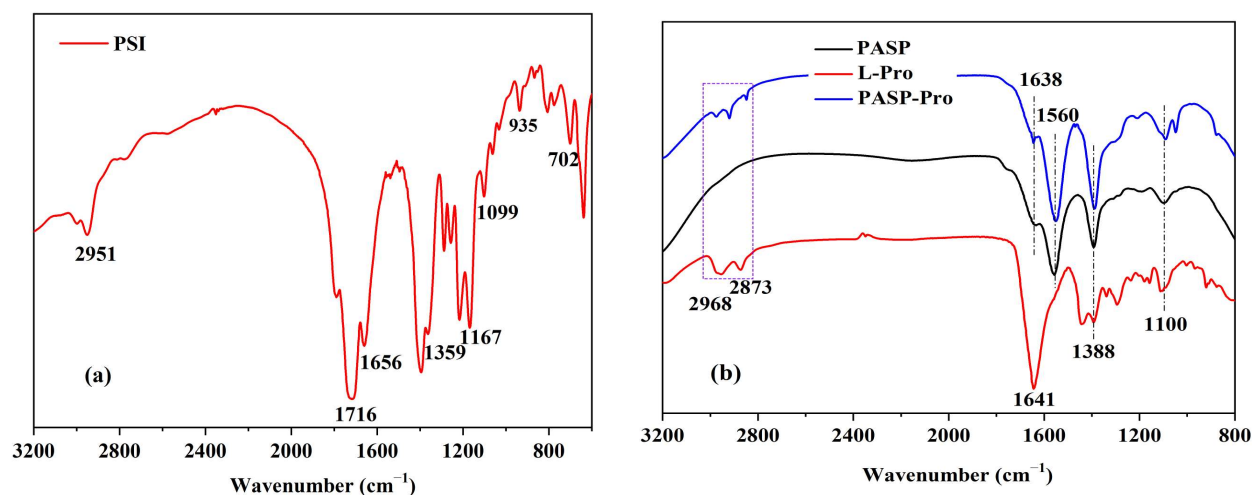


**Figure 2.** FTIR spectra of PSI, L-Pro, PASP, and PASP-Pro on the synthetic route. PSI (a); L-Pro, PASP, and PASP-Pro (b).

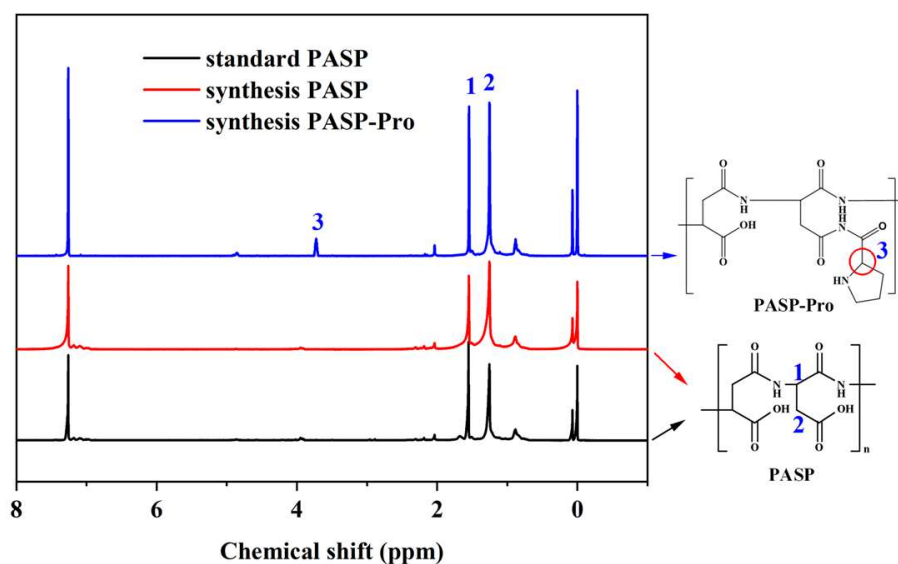


**Figure 3.**  $^1\text{H}$  NMR spectra of PASP and PASP-Pro.

The FTIR spectra and  $^1\text{H}$  NMR spectra confirmed that the introducing molecule L-Pro was successfully grafted into the framework of PASP, and PASP-Pro was successfully synthesized.

Figure 4 shows the retention time of synthesized PSI and PASP and PASP-Pro with different ring-opening reaction times in sodium hydroxide solution, and Table 1 shows the  $M_w$  calculated from the GPC measurement. It can be seen that the molecular weight of PSI is 15,661 Da, and the molecular weight of PASP and PASP-Pro obtained by the ring-opening reaction is smaller than that of PSI and becomes lower with the prolongation of ring-opening time under alkaline conditions, and the minimum molecular weight decreases to about 1200~1300 Da. At the same ring-opening reaction time, the molecular weight of PASP-Pro is higher than that of PASP. If the same degree of breaking of the  $-\text{NH}-\text{CO}-$  bonds on the polymer occurs, the higher molecular weight of PASP-Pro means the successful grafting of L-Pro.

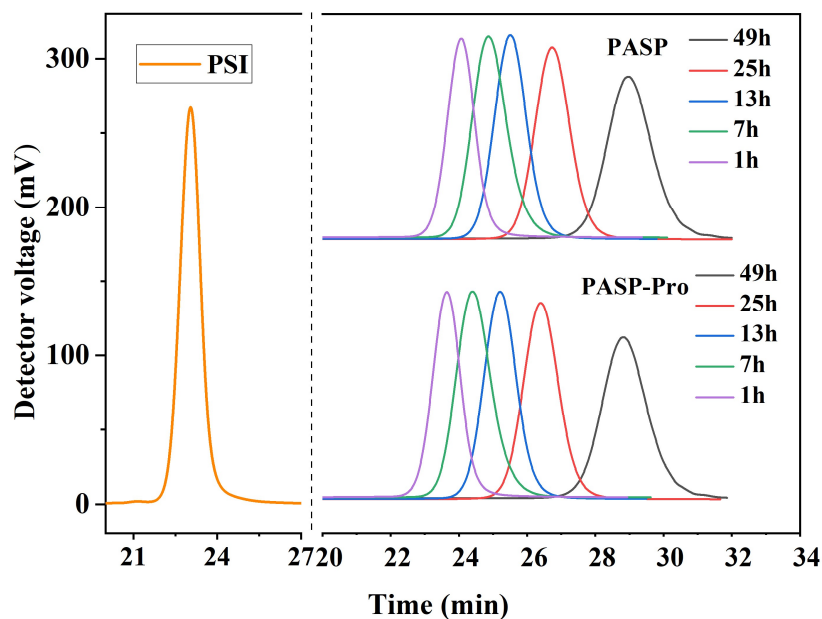


Figure 4. GPC of PSI, PASP, and PASP-Pro.

Table 1. Data resulting from GPC analysis for PSI, PASP, and PASP-Pro.

Ring-Opening Reaction Time (h)	PSI $M_w$ (g/mol)	PASP $M_w$ (g/mol)	PASP-Pro $M_w$ (g/mol)
1	15,661	8733	9468
7		5678	6846
13		4106	4751
25		2456	3012
49		1190	1328

### 3.2. Inhibition Performance of PASP-Pro on the $CaCO_3$ Scale

Figure 5a shows the effects of the ring-opening time on the scale inhibition performance of the PASP and PASP-Pro. When the ring-opening time is less than 13 h, the scale inhibition rate increases with the extension of the ring-opening time; however, the scale inhibition performance decreases slightly after the ring-opening time exceeds 13 h. The reduction in the scale inhibition rate of PASP-Pro is lower than that of PASP. The ring-opening reaction time can directly affect the molecular weight of the synthesized PASP-based scale inhibitors. When the reaction time is short, the PSI ring-opening reaction mainly occurs and the molecular weight of the synthesized PASP is large; when the reaction time is long enough, the amide bonds on the main chain of the PASP are broken, resulting in a large number of PASPs with short chain lengths. As we know, the corresponding molecular weight is related to the best scale inhibition performance; PASP and PASP-Pro showed the best scale inhibition performance when the ring-opening time is about 13–25 h. The corresponding molecular weights are 2456 to 4610 and 3012 to 4751, which are basically consistent with those reported in the literature [30].

When the concentration of scale inhibitors is in a wide range of 4–20 mg/L, the scale inhibition rate of PASP remains above 90% (Figure 5b). The slight decrease in the scale inhibition rate may be attributed to the concentration of the scale inhibitors exceeding calcium tolerance [31,32]. A few PASP and  $Ca^{2+}$  can probably form a complex precipitate, which leads to the reduction in the  $Ca^{2+}$  concentration in the solution. In addition, the inhibition rate increases with the increase in the concentration of PASP-Pro, and it remains nearly constant (95%) when the  $Ca^{2+}$  concentration is beyond 16 mg/L, which reveals that the modified PASP-Pro has a higher calcium tolerance.

The scale inhibition performance of PASP and PASP-Pro are very close in pH, ranging from 6–8 (Figure 5c). However, the scale inhibition rate rapidly dropped to 40% when the pH exceeds 9, which is probably because the alkalinity promotes the conversion of  $\text{HCO}_3^-$  to  $\text{CO}_3^{2-}$ . Similarly, PASP and PASP-Pro are not much different in scale inhibition rate when increasing the concentration of  $\text{Ca}^{2+}$ ; the scale inhibition performance only drops slightly in the range of  $\text{Ca}^{2+}$  concentration from 120 mg/L to 720 mg/L (Figure 5d).

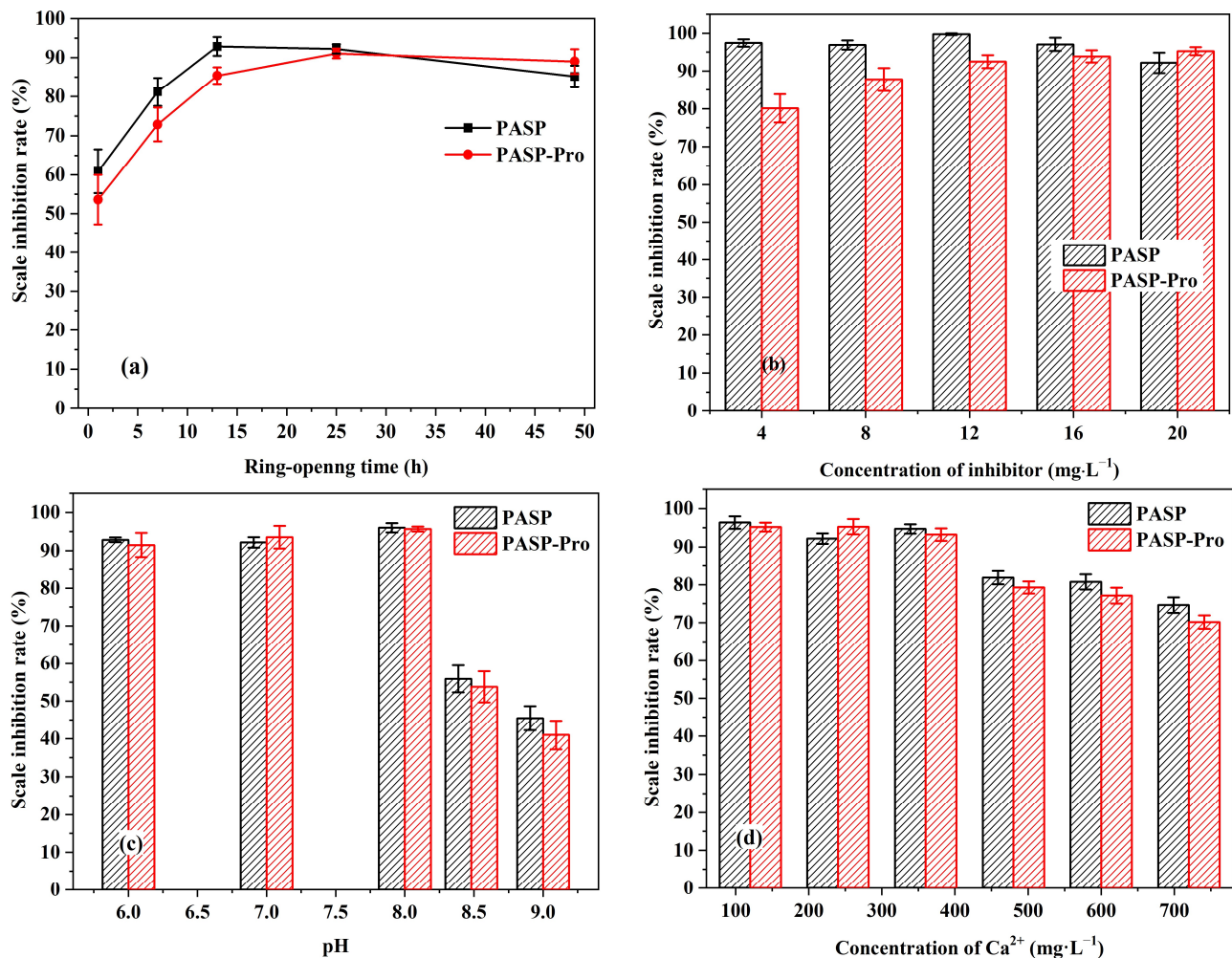


**Figure 5.** The effects of ring-opening time (a); concentration of inhibitors (b); pH (c); and concentration of  $\text{Ca}^{2+}$  (d) on scale inhibition rate. Static experiment details: ring-opening time of the inhibitors is 25 h,  $\rho(\text{Ca}^{2+}) = 240$  mg/L and  $\rho(\text{HCO}_3^-) = 732$  mg/L in artificial solution, pH = 7, the concentration of the inhibitors is 20 mg/L, bath temperature is 80 °C, and bath time is 10 h, except for the variables in each experiment.

### 3.3. Thermal Stability of PASP-Pro

#### 3.3.1. Effect of Bath Temperature and Bath Time

The difference between PASP and PASP-Pro is clearly distinguished by the influence of bath temperature and bath time on the scale inhibition performance. Figure 6a shows that the scale inhibition performance of PASP-Pro is better than that of PASP as the water bath temperature is higher than 70 °C. Moreover, the scale inhibition rate of PASP-Pro is significantly greater than that of PASP with the increasing bathing time (Figure 6b), and it still reaches 85% at 20 h of the bath time, which proves that PASP-Pro still has good scale inhibition performance when exposed to high temperatures for a long time. The actual temperature of the scale inhibitor in geothermal water is often higher than 80 °C in the static test, and the scale inhibitor is often difficult to continuously replenish. Considering the

higher scale inhibition temperature and longer scale inhibition time, the modified PASP-Pro has more practical advantages.

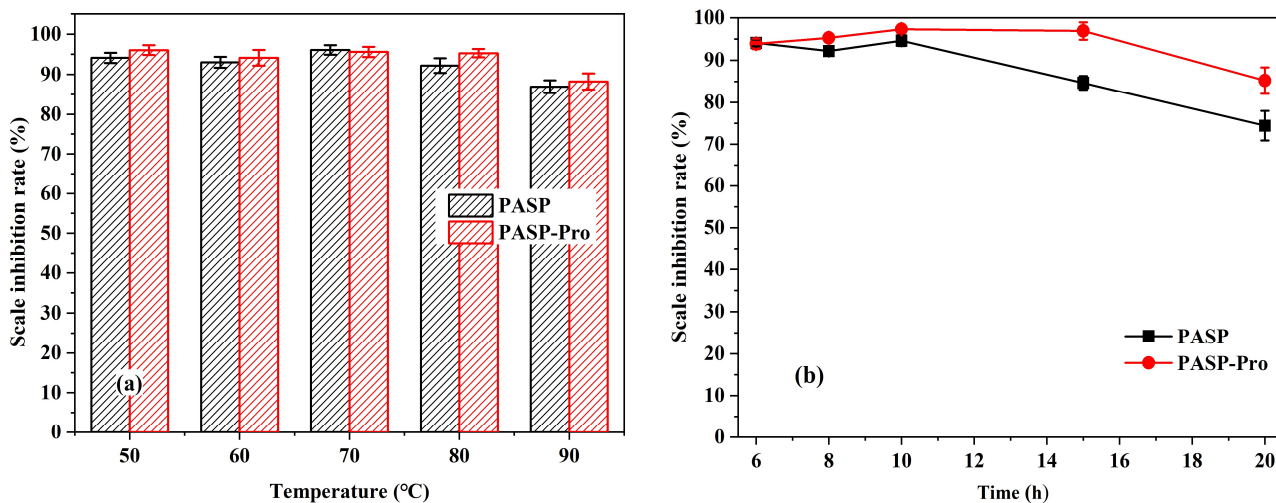


Figure 6. The effect of bath temperature (a) and bath time (b) on scale inhibition rate.

### 3.3.2. Effects of Heat Treatment Temperature

The scale inhibition performance of PASP-Pro is much higher than that of PASP after heat treatment at 110–170 °C (Figure 7a). At 110 °C, the scale inhibition rate of PAPS-Pro exceeds 90%, which is almost as high as without heat treatment. After heat treatment at 150 °C, the scale inhibition rate is still higher than 87%, which is significantly higher than the scale inhibition rate of PASP (74%) at the same heat treatment temperature. When the heat treatment temperature is increased to 170 °C, the scale inhibition rate of PASP-Pro decreases significantly and becomes unable to meet the use requirements. However, it is worth noting that the temperature of common geothermal well water is lower than this value, which means that PASP-Pro still has a broad application prospect in geothermal water.

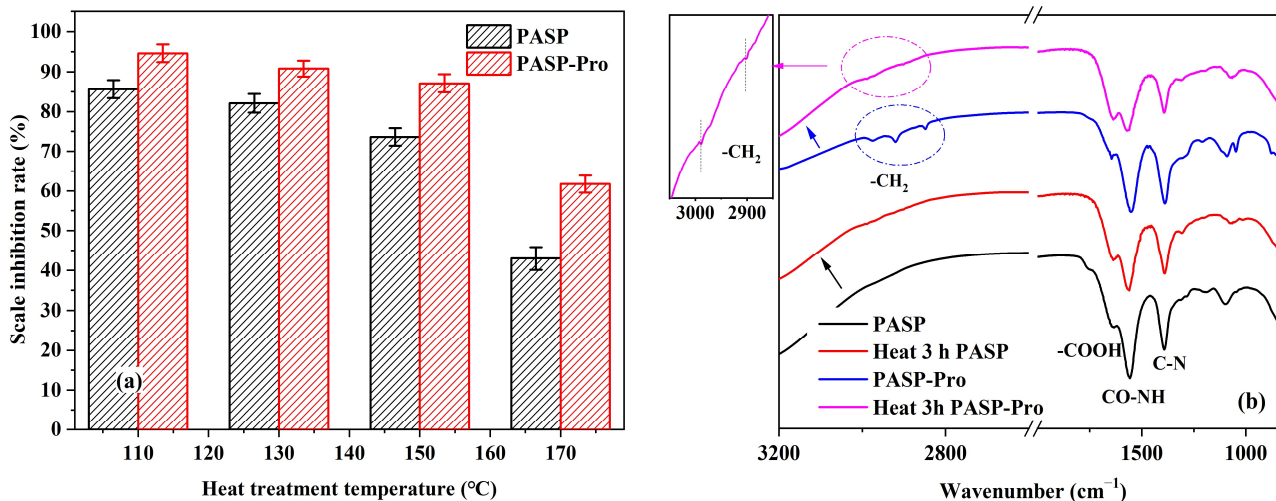


Figure 7. The relationship between scale inhibition rate and heat treatment temperature (a); FTIR of scale inhibitors after heat treatment (b).

It can be seen from Figure 7b that the strength of the amide group in PASP is significantly reduced, which means that the main chain of PASP is broken, whereas the strength of the amide group and the grafted methyl in PASP-Pro are still intact after heat treatment. After the amidation reaction between L-Pro and PASP, the steric hindrance of the PASP-Pro

segment increases; at the same time, new hydrogen bonds are generated between atoms such as O and N, which can promote the stability of PASP-Pro at high temperatures.

### 3.4. Scale Inhibition Mechanism

#### 3.4.1. The influence of PASP-Pro on the Nucleation Process of CaCO<sub>3</sub>

In general, the CaCO<sub>3</sub> nucleation process can be divided into three stages: induction period, nucleation period, and crystal growth period [33]. During the nucleation period, the conductivity of the critical supersaturation CaCO<sub>3</sub> solution dropped rapidly. As time went by, the conductivity decreased slowly to a stable value; the constant conductivity value in the growth period is related to the rearrangement and growth of the CaCO<sub>3</sub> nucleus. Figure 8 shows the conductivity change in the solutions containing CaCl<sub>2</sub> and Na<sub>2</sub>CO<sub>3</sub>, which is clearly distinguished from the absence or presence of scale inhibitors. In comparison, the addition of scale inhibitors significantly prolonged the induction period and nucleation period, indicating that the migration of ions in the solution occurs slowly, which may be related to a large amount of negatively charged functional groups in PASP and PASP-Pro. This reveals that scale inhibitors also hinder the formation of ACC. In addition, the conductivity value in the final stage of solution after adding PASP-Pro is higher than that of PASP, with more free ions in the solution indicating that there are fewer Ca<sup>2+</sup> and CO<sub>3</sub><sup>2-</sup> ions participating in the formation of crystal nuclei in the solution.

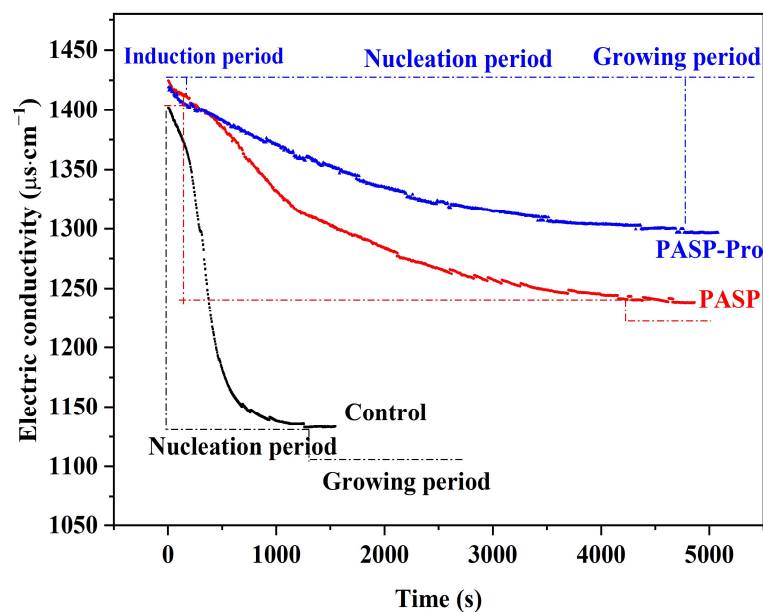


Figure 8. The conductivity changes with time in the nucleation process of CaCO<sub>3</sub>.

#### 3.4.2. The Influence of PASP-Pro on the Morphology of CaCO<sub>3</sub> Scale

Figure 9 shows the structures of CaCO<sub>3</sub> scale crystals by XRD. The diffraction peaks at  $2\theta = 23.1^\circ$ ,  $29.4^\circ$ ,  $36.0^\circ$ , and  $39.4^\circ$  correspond to calcite. This demonstrates that only calcite is formed in the absence of the scale inhibitors; however, the characteristic peaks of vaterite at  $24.9^\circ$ ,  $27.0^\circ$ , and  $32.8^\circ$  can also be found in the presence of PASP or PASP-Pro, but there are obvious differences in the intensity of vaterite characteristic peaks between PASP-Pro and PASP. The characteristic peak intensity of vaterite was lower when PASP-Pro was added. We used jade 6.5 to calculate the relative content of various crystals of calcium carbonate, and the results are shown in Table 2. Calcium carbonate added with PASP and PASP-Pro has 65.47% and 5.89% relative content of aragonite, respectively. Calcite crystal is the most thermodynamically stable crystal, while vaterite crystal is the most unstable [34]. The addition of PASP and PASP-Pro scale inhibitors effectively prevents the generation of stable scale and promotes the conversion of CaCO<sub>3</sub> nuclei to vaterite. This is most likely

because the scale inhibitors adsorbed on the crystal surface cause lattice distortion and then affect the path of ACC to calcite, thus changing the structure of the  $\text{CaCO}_3$  scale.

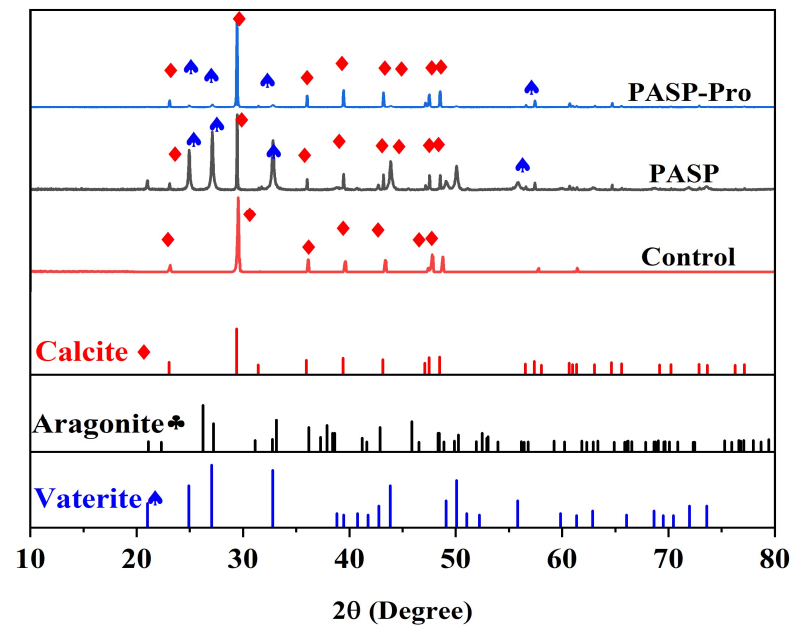


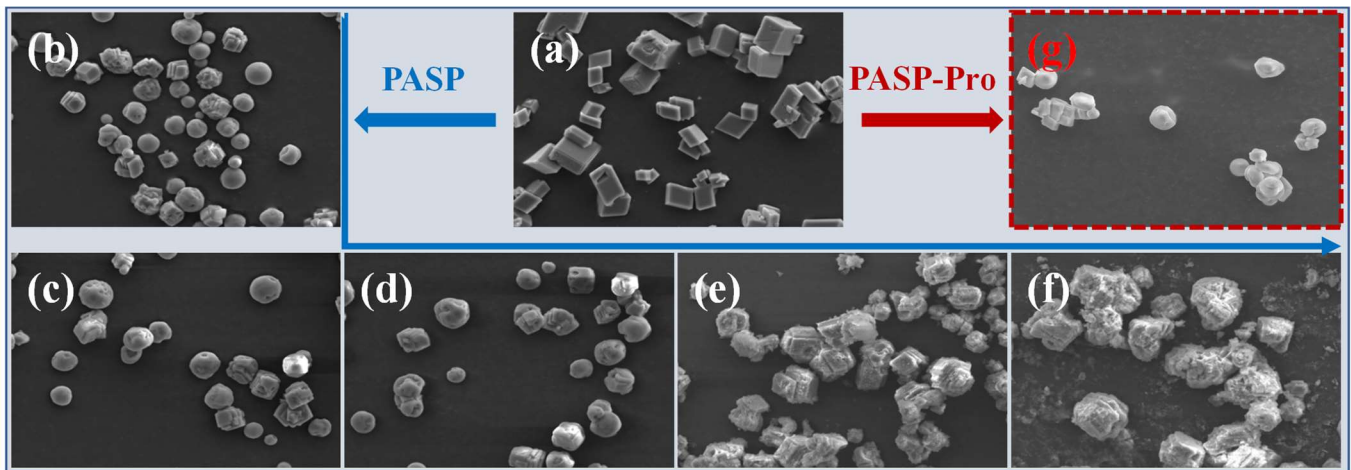
Figure 9. The XRD patterns of the  $\text{CaCO}_3$  crystals.

Table 2. Relative content of calcium carbonate crystal.

Relative Content (%)	Calcite	Aragonite	Vaterite
Control	100%	0.00%	0.00%
PASP	34.32%	0.21%	65.47%
PASP-Pro	93.37%	0.74%	5.89%

The change in the  $\text{CaCO}_3$  crystals' morphology was identified by SEM to investigate the underlying mechanism of the additives hindering scaling. In the absence of a scale inhibitor, the formed crystals with the regular cube and smooth surfaces can be found in Figure 10a; they are the morphologies of calcite. After adding the scale inhibitors, all  $\text{CaCO}_3$  scales had a loose structure, and the particle size did not change significantly with the addition of different scale inhibitors. However, with the addition of PASP having different ring-opening times, the morphology of regular  $\text{CaCO}_3$  crystals gradually changes (Figure 10b–f). Many particles with a spherical structure that correspond to vaterite can be observed while PASP shows a relatively short ring-opening time (1–13 h). When the ring-opening time of PASP exceeds 25 h, it can be found that the edges and corners of the formed calcites are destroyed. A lot of loose fine particles are attached to the  $\text{CaCO}_3$  surface, and this change becomes more obvious after the ring-opening time of PASP reaches 49 h; the initial cubes are almost difficult to distinguish. As we know, the ring-opening time is directly related to the molecular weight of PASP, and a short ring-opening time promotes the generation of a large molecular weight of PASP. A small number of PASPs with long chains can be adsorbed on multiple sites of the initial nucleus of  $\text{CaCO}_3$ , making the nucleus of  $\text{CaCO}_3$  more likely to be converted into vaterite. However, with the extension of the ring-opening reaction time, a large number of PASPs with short chains can adsorb onto the surfaces of  $\text{CaCO}_3$  and would prevent crystals from growing based on the electrostatic repulsion, leading to the formation of irregular crystals.

The effect of PASP-Pro on the morphology of calcium carbonate is similar to PASP, and spherical vaterite particles (Figure 10g) can also be observed, which is consistent with the XRD characterization results.



**Figure 10.** The effect of scale inhibitors on  $\text{CaCO}_3$  scale. Without (a); 1 h (ring-opening time) PASP (b); 7 h PASP (c); 13 h PASP (d); 25 h PASP (e); 49 h PASP (f); and 25 h PASP-Pro (g).

### 3.4.3. Possible Multi-Stage Scale Inhibition Mechanism of PASP-Based Scale Inhibitors

In the static test, high pH, high temperature, and high supersaturation significantly reduced the scale inhibition performance of PASP-based scale inhibitors for  $\text{CaCO}_3$ . The induction period and nucleation period of  $\text{CaCO}_3$  are greatly prolonged and the formation of vaterite with a loose structure was observed after adding scale inhibitors. Combining the above results with the existing scale inhibition theory, the multi-stage scale inhibition mechanism of PASP-based scale inhibitors was proposed as follows.

In this work, the  $\text{CaCO}_3$  crystallization process is considered a primary heterogeneous nucleation process. When no scale inhibitors are added, an amorphous ionic liquid composed of alternate  $\text{Ca}^{2+}$  and  $\text{CO}_3^{2-}$  adsorbs on the positively charged sites of the impurities that are present in the solution, and then collapses and triggers the subsequent nucleation stages to form stable calcite. After adding PASP-based scale inhibitors, they are more likely to be adsorbed on the surface of impurities due to the electronegative functional groups ( $-\text{COOH}$  and  $-\text{CO-NH-}$ ). The  $\text{CaCO}_3$  crystallization process would be closer to occurring in pseudo-homogeneous solution when most of the active sites of impurities were covered. Therefore, the subsequent nucleation only occurs under more stringent conditions such as high temperature, high pH, or high saturation.

In addition, PASP-based scale inhibitors are easily introduced into amorphous ionic liquid due to chelation with  $\text{Ca}^{2+}$  by the strong adsorptive capacity; this would slow down ion migration by increasing the dielectric constant and electrostatic repulsion, prolonging the induction period and the nucleation period of ACC nanospheres. The adsorption of scale inhibitors on the surface of ACC would also cause lattice distortion and inhibit the conversion from ACC to the calcite phase.

Furthermore, the dehydration and local ordering process of ACC are limited due to the introduction of PASP-based scale inhibitors. Small amounts of scale inhibitors and water molecules remain inside the crystals, resulting in a loose and coarse crystal surface structure. The details of multi-stage anti-scaling with or without PASP-based scale inhibitors are illustrated in Figures 11 and 12.

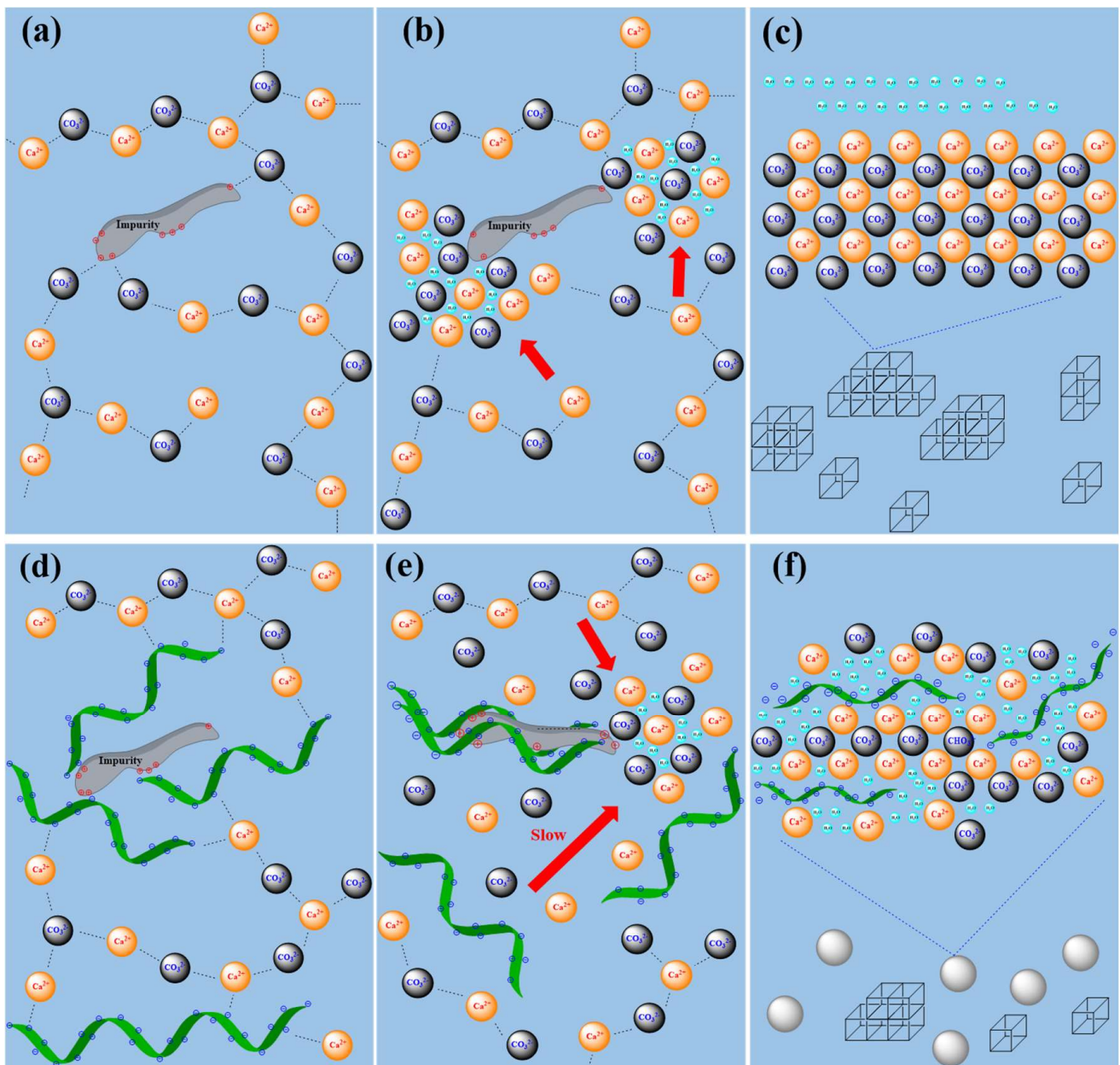


**Figure 11.** The schematic diagram of multi-stage nucleation. Ionic liquid polymer collapse and dehydration in the absence of PASP (a–c); in the presence of PASP (d–f).

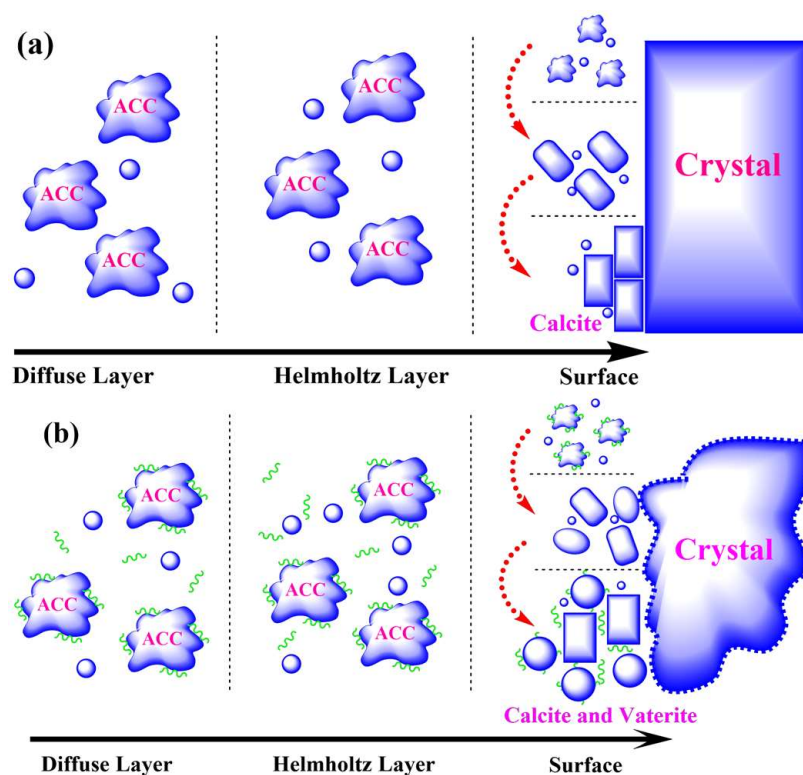


**Figure 12.** The schematic diagram of ACC conversion. In the absence of a PASP (a); in the presence of PASP (b).

#### 4. Conclusions

PASP and PASP-Pro as scale inhibitors for geothermal circulating water in high temperatures were successfully synthesized. The best conditions of synthesis and evaluation conditions of PASP-Pro were explored by static tests. Moreover, the static tests and thermal stability tests of PASP-Pro were established to investigate the performance of PASP-Pro in high temperatures. Conductivity experiments, XRD, and SEM characterization were used to explore the mechanism of scale inhibition. The following conclusions are summarized:

1. The high-temperature scale inhibition performance and thermal stability of PASP-Pro are significantly better than that of PASP.
2. Adding scale inhibitors significantly prolonged the induction period and nucleation period of  $\text{CaCO}_3$  nucleation, and more free ions can be stable in the solution. Unstable vaterite was found in the presence of scale inhibitors and  $\text{CaCO}_3$  crystals are no longer smooth and dense after adding PASP or PASP-Pro.
3. The scale inhibition mechanism speculated in this paper: PASP-based scale inhibitors cover the nucleation sites of impurity in the  $\text{CaCO}_3$  solution and are introduced into the amorphous ionic liquid. Then, they hinder the growth of ACC through electrostatic repulsion and inhibit the dehydration and local ordering of ACC to achieve the effect of inhibiting  $\text{CaCO}_3$  scaling.

**Author Contributions:** Conceptualization, S.Q.; methodology, J.Y.; validation, J.Y. and X.T.; formal analysis, J.Y.; investigation, S.Q., J.Y., and X.T.; resources, S.Q.; data curation, J.Y.; writing—original draft preparation, S.Q. and J.Y.; writing review and editing, S.Q. and J.Y.; supervision, X.T.; project administration, S.Q. All authors have read and agreed to the published version of the manuscript.

**Funding:** This research was funded by the National Natural Science Foundation of China (22038011) and the Natural Science Foundation of Shaanxi Province (2020JM-061).

**Data Availability Statement:** The datasets generated and/or analyzed during the current study are not publicly available.

**Acknowledgments:** Many thanks to the editors and anonymous reviewers for providing valuable comments that significantly improved this paper.

**Conflicts of Interest:** The authors declare no conflict of interest.

## References

1. Lund, J.W.; Boyd, T.L. Direct utilization of geothermal energy 2015 worldwide review. *Geothermics* **2016**, *60*, 66–93. [[CrossRef](#)]
2. Soltani, M.; Kashkooli, F.M.; Souri, M.; Rafiei, B.; Jabarifar, M.; Gharali, K.; Nathwani, J.S. Environmental, economic, and social impacts of geothermal energy systems. *Renew. Sustain. Energy Rev.* **2021**, *140*, 110750–110762. [[CrossRef](#)]
3. Nasruddin; Alhamid, M.I.; Daud, Y.; Surachman, A.; Sugiyono, A.; Aditya, H.B.; Mahlia, T.M.I. Potential of geothermal energy for electricity generation in Indonesia: A review. *Renew. Sustain. Energy Rev.* **2016**, *53*, 733–740. [[CrossRef](#)]
4. Griebl, C.; Briemann, H.; Haberer, C.M.; Kaschuba, S.; Kellermann, C.; Stumpp, C.; Hegler, F.; Kuntz, D.; Walker-Hertkorn, S.; Lueders, T. Potential impacts of geothermal energy use and storage of heat on groundwater quality, biodiversity, and ecosystem processes. *Environ. Earth Sci.* **2016**, *75*, 1391–1403. [[CrossRef](#)]
5. Li, Y.; Liu, Y.; Hu, B.; Dong, J. Numerical investigation of a novel approach to coupling compressed air energy storage in aquifers with geothermal energy. *Appl. Energy* **2020**, *279*, 115781–115799. [[CrossRef](#)]
6. Guzovic, Z.; Majcen, B.; Cvetkovic, S. Possibilities of electricity generation in the Republic of Croatia from medium-temperature geothermal sources. *Appl. Energy* **2012**, *98*, 404–414. [[CrossRef](#)]
7. Li, Y.M.; Pang, Z.H. Carbonate Calcium Scale Formation and Quantitative Assessment in Geothermal System. *Adv. New Renew. Energy* **2018**, *4*, 274–281.
8. Cosmo, R.; Pereira, F.; Soares, E.J.; Ferreira, E.G. Addressing the root cause of calcite precipitation that leads to energy loss in geothermal systems. *Geothermics* **2022**, *98*, 102272–102284. [[CrossRef](#)]
9. Ma, Z.Y.; Yan, H.; Zhou, X.; Hou, C. Impact of Carbonate Scaling on the Efficiency of Used Geothermal Water Reinjection from Low-Middle Temperature Geothermal Fluid in Xianyang Porous Geothermal Field, NW China. *AMR* **2013**, *614–615*, 307–310. [[CrossRef](#)]
10. Chaussemier, M.; Pourmohtasham, E.; Gelus, D.; Pécou, N.; Perrot, H.; Lédion, J.; Cheap-Charpentier, H.; Horner, O. State of art of natural inhibitors of calcium carbonate scaling. A review article. *Desalination* **2015**, *356*, 47–55. [[CrossRef](#)]
11. Hasson, D.; Shemer, H.; Sher, A. State of the Art of Friendly “Green” Scale Control Inhibitors: A Review Article. *Ind. Eng. Chem. Res.* **2011**, *50*, 7601–7607. [[CrossRef](#)]
12. Xu, Y.; Zhang, B.; Zhao, L.; Cui, Y. Synthesis of polyaspartic acid/5-aminoorotic acid graft copolymer and evaluation of its scale inhibition and corrosion inhibition performance. *Desalination* **2013**, *311*, 156–161. [[CrossRef](#)]
13. Shi, S.; Zhao, X.; Wang, Q.; Shan, H.; Xu, Y. Synthesis and evaluation of polyaspartic acid/furfurylamine graft copolymer as scale and corrosion inhibitor. *RSC Adv.* **2016**, *6*, 102406–102412.
14. Shen, Z.; Xin, Z.; Zhang, P. Preparation of fluorescent polyaspartic acid and evaluation of its scale inhibition for CaCO<sub>3</sub> and CaSO<sub>4</sub>. *Polym. Adv. Technol.* **2017**, *28*, 323–336. [[CrossRef](#)]
15. Belcher, A.M.; Christensen, R.J.; Hansma, P.K.; Stucky, G.D.; Morse, D.; Wu, X.H. Control of crystal phase switching and orientation by soluble mollusc-shell proteins. *Nature* **1996**, *381*, 56–58. [[CrossRef](#)]
16. Aizenberg, J.; Tkachenko, A.; Weiner, S.; Addadi, L.; Hendler, G. Calcitic microlenses as part of the photoreceptor system in brittlestars. *Nature* **2001**, *412*, 819–822. [[CrossRef](#)] [[PubMed](#)]
17. Albéric, M.; Bertinetti, L.; Zou, Z.; Fratzl, P.; Habraken, W.; Politi, Y. The Crystallization of Amorphous Calcium Carbonate is Kinetically Governed by Ion Impurities and Water. *Adv. Sci.* **2018**, *26*, 1701000–1701014. [[CrossRef](#)] [[PubMed](#)]
18. Yoreo, J.D.; Sommerdijk, N. Investigating materials formation with liquid-phase and cryogenic TEM. *Nat. Rev. Mater.* **2016**, *1*, 16035–16047. [[CrossRef](#)]
19. Demichelis, R.; Raiteri, P.; Gale, J.D.; Quigley, D.; Gebauer, D. Stable prenucleation mineral clusters are liquid-like ionic polymers. *Nat. Commun.* **2011**, *2*, 590–604. [[CrossRef](#)]
20. Prus, M.; Szymanek, K.; Mills, J.; Lammers, L.N.; Piasecki, W.; Kedra-Krolik, K.; Zarzyck, P. Electrophoretic and potentiometric signatures of multistage CaCO<sub>3</sub> nucleation. *J. Colloid Interface Sci.* **2019**, *544*, 249–256. [[CrossRef](#)]
21. Chen, J.; Xu, H.; Han, J.; Wang, C.; Wu, Q.; Li, C. A green multifunctional anti-scaling inhibitor for crystallization control of Ca scale crystals. *Chem. Eng. Technol.* **2018**, *42*, 444–453. [[CrossRef](#)]
22. Zhang, B.R.; Zhang, L.; Li, F.T.; Hu, W.; Hannam, P.M. Testing the formation of Ca-phosphonate precipitates and evaluating the anionic polymers as Ca-phosphonate precipitates and CaCO<sub>3</sub> scale inhibitor in simulated cooling water. *Corros. Sci.* **2010**, *52*, 3883–3890. [[CrossRef](#)]
23. Sheikhi, A.; Na, L.; Mejlse, S.L.; Bomal, E.; Kakkar, A. Rational design of molecularly engineered biomimetic threshold scale inhibitors. *J. Mater. Chem. A* **2018**, *6*, 24058–24065. [[CrossRef](#)]
24. Chen, S.; Xu, X.; Hou, X.Y.; Wu, D.X.; Yin, J.H. Molecular weight effect on PAA antiscaling performance in LT-MED desalination system: Static experiment and MD simulation. *Desalination* **2018**, *445*, 1–5.
25. Chen, J.; Xu, L.; Han, J.; Su, M.; Wu, Q. Synthesis of modified polyaspartic acid and evaluation of its scale inhibition and dispersion capacity. *Desalination* **2015**, *358*, 42–48. [[CrossRef](#)]

26. Huang, H.H.; Yao, Q.; Jiao, Q.; Liu, B.L.; Chen, H.L. Polyepoxysuccinic acid with hyper-branched structure as an environmentally friendly scale inhibitor and its scale inhibition mechanism. *J. Saudi Chem. Soc.* **2019**, *23*, 61–74. [[CrossRef](#)]
27. Xu, Y.; Zhao, L.L.; Wang, L.N.; Xu, S.Y.; Cui, Y.C. Synthesis of polyaspartic acid–melamine grafted copolymer and evaluation of its scale inhibition performance and dispersion capacity for ferric oxide. *Desalination* **2012**, *286*, 285–289. [[CrossRef](#)]
28. Zhang, Z.J.; Lu, M.L.; Liu, J.; Chen, H.L.; Chen, Q.L.; Wang, B. Fluorescent-tagged hyper-branched polyester for inhibition of CaSO<sub>4</sub> scale and the scale inhibition mechanism. *Mater. Today Commun.* **2020**, *25*, 101359. [[CrossRef](#)]
29. Zhang, S.P.; Qu, H.J.; Yang, Z.; Fu, F.E.; Tian, Z.Q.; Yang, W.B. Scale inhibition performance and mechanism of sulfamic/amino acids modified polyaspartic acid against calcium sulfate. *Desalination* **2017**, *419*, 152–159. [[CrossRef](#)]
30. Ross, R.J.; Low, K.; Shannon, J.E. Polyaspartate scale inhibitors—Biodegradable alternatives to polyacrylates. *Mater. Perform.* **1997**, *38*, 53–57.
31. Rong, Y.U.; Ma, Z.X.; Zhou, X.; Su, L.L.; Tang, Z.; Li, Z.H. Study on Scale Inhibition Performance of AA-MA-HEMA Scale Inhibitor. *Contemp. Chem. Ind.* **2018**, *47*, 6–16.
32. Jitreewas, P.; Saengvattanasat, S.; Tansiri, P.; Pranee, S.; Chuayprakong, S.; Khemtong, C.; Seeyangnok, S. Synthesis of PAA-PAMPS-PNaSS Terpolymers as Ultraviolet-Tagged Scale Inhibitor for Industrial Water Cooling System. *Key Eng. Mater.* **2017**, *16*, 757–786. [[CrossRef](#)]
33. Rahman, F. Calcium sulfate precipitation studies with scale inhibitors for reverse osmosis desalination. *Desalination* **2013**, *319*, 79–84. [[CrossRef](#)]
34. Mady, M.F.; Kelland, M.A. A Study on Various Readily Available Proteins as New Green Scale Inhibitors for Oilfield Scale Control. *Energy Fuels* **2017**, *31*, 5940–5947. [[CrossRef](#)]

**Disclaimer/Publisher’s Note:** The statements, opinions and data contained in all publications are solely those of the individual author(s) and contributor(s) and not of MDPI and/or the editor(s). MDPI and/or the editor(s) disclaim responsibility for any injury to people or property resulting from any ideas, methods, instructions or products referred to in the content.